Electronic Supplementary Material of

Approaching Phase-Imaging through Defocusing Shadowgraphy for Acoustic-Resonators Diagnosis, and the Capability of Direct IoR Measurements

Yi You* and Jens Riedel
Federal Institute for Materials Research and Testing (BAM), Berlin, D-12489, Germany

Corresponding author: Yi You, Email: yi.you@bam.de

Table of Contents

1. Extended Experimental Information

Sample gas source

In this work, two types of gases were used: chemical vapors carried by ambient air and pure gases (Figure S1). For both cases, the outlet capillary was the same. Essentially, a laminar flow stream was desired. In specific, the vapor-based gas streams were generated with a mixing chamber (Figure S1a). The ambient air was pumped into the chamber through a direct-current diaphragm pump at ~0.4 L min^{-1}. The carrying gas, *i.e.* ambient air, was not bubbled through the sample liquid to avoid supersaturation. When the refractive indices were estimated, the vapor pressures of liquid samples were used. In the other case where pure gas was used, the diaphragm pump was replaced by direct gas sources (*e.g.*, argon, CO_2) and a buffering balloon to maintain the positive pressure (Figure S1b). Instead of regulating the output flow rate with the diaphragm pump, a home-made pinch valve was added before the outlet capillary to ensure a laminar flow near the outlet. The flow rate was not controlled with a feedback loop. Once a laminar pattern was observed on the real-time image, the flowrate was set. A back calibration was performed with a standard flow calibrator (Gillibrator 2, Gillian) to measure the exact flow rate at the outlet capillary.

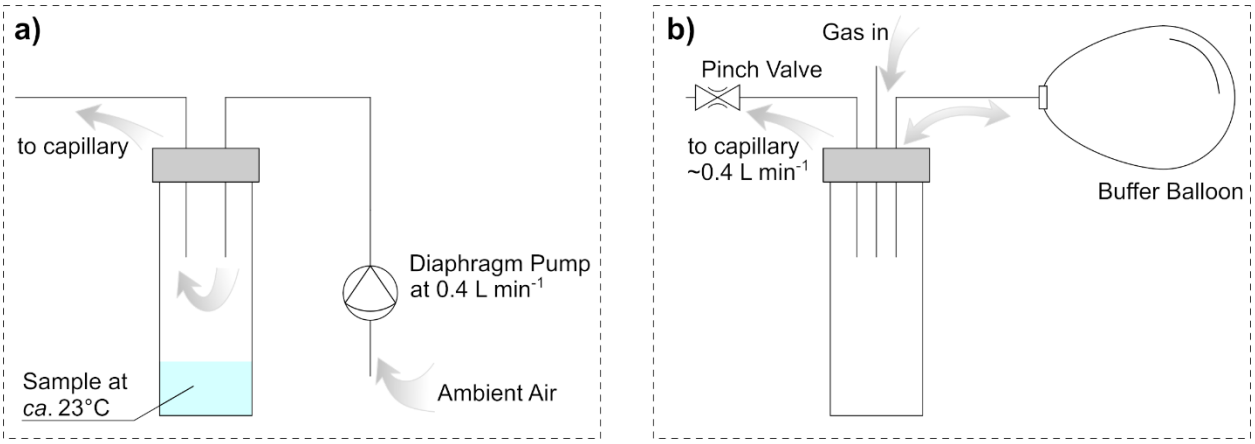

Figure S 1. Geometries of the gas supply chain. The vapor-based gas stream and pure gas stream generators are shown in (a) and (b), respectively.

Light source

The blue light was provided by a three-color light-emitting diode (LED, 5 mm OD, unknown manufacture). Only the blue component of the LED was used in this work, whereas the green and red ones remained off. This LED was selected because a monochrome camera was used. Namely, we were unable to extract the wavelength information through the Bayer filter as it is available on a color camera. In a future work, we will exploit the wavelength information for further quantitative analyses. The emission spectrum of the LED (Figure S2) was superimposed by spectra for each LED component. All emission spectra were recorded with a Czerny-Turner spectrometer (i303 – iDus 420CCD, Andor, Belfast, UK).

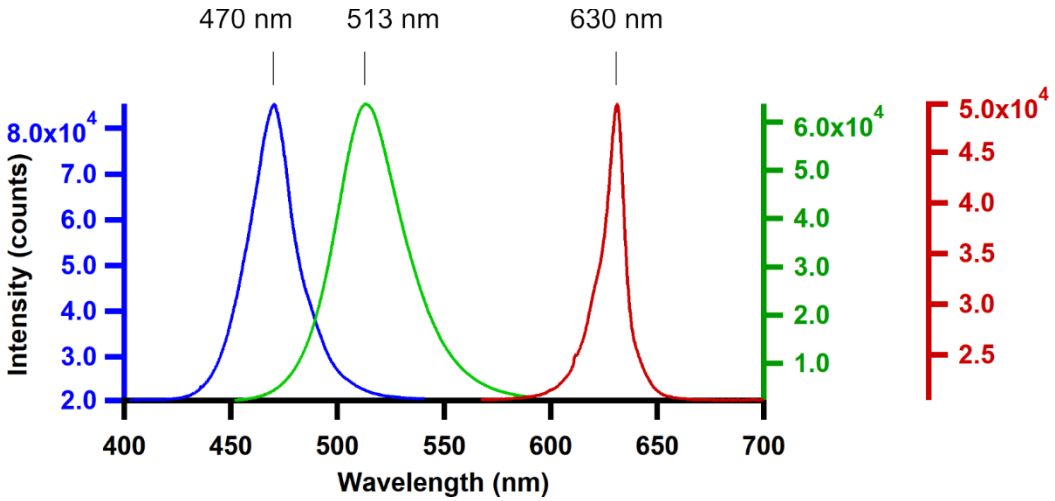

Figure S 2. Superimposed emission spectrum of the light source.

LED pulse driver

In contrast to common current-controlled drivers for LEDs with a feedback loop, a crude version was used in this work for measurements under the synchronous mode. Without the current feedback loop, the LED current was controlled through the MOSFET by tuning the gate voltage. A Schmitt-trigger type MOSFET gate driver (MC34151) was used, which can be operated into low MHz bands. The supply voltage of the gate driver, V_{dd}, dictated the current through the LED. The output signal from the digital-delay generator (DDG, DG-645) was transferred to the LED driver board through a coaxial cable (RG174); the signal was terminated by a 50 Ω resistor. A separate voltage source for the LED loop was coupled through a Π-type low-pass filter to avoid high-frequency interference between the LED switching operation and the switch-mode power supply (SMPS) itself. The LED supply voltage, V_{cc}, was set to 3.5 V for the blue component used in this case.

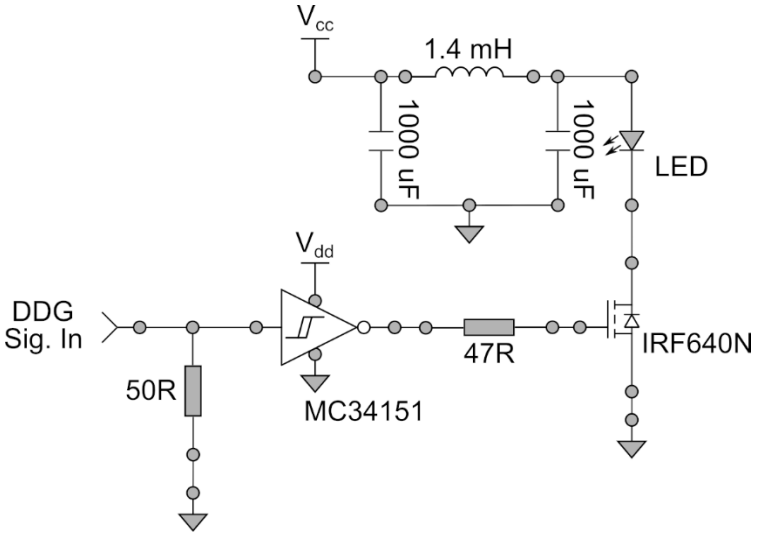

Figure S 3. Home-made crude pulse LED driver.

The optical emission from the LED was too weak to be detected with a simple photo-sensing diode (or PIN diode). Thus, no optical-output characterization was performed for the LED. Instead, the diode recovery time (10%-90%) was experimentally determined to be *ca*. 50 ns for the LED used in this study. From the recorded images under the synchronous mode, we assume the temporal parameters, *e.g.*, pulse duration, jitter, etc., did not clutter the final images. However, if synchronous-mode acquisitions are to be performed in higher frequency ranges, *e.g.*, HF or VHF, the temporal emissions characterization for the LED will be necessary.

2D acoustic-resonator driver

While the 1D acoustic resonator was commercially available, the 2D one was fully built in-house. Aside from the supporting frame, the driver circuit was designed specifically for the acoustic resonator demonstrated in Figure 3 of the main text. For simplicity, the detailed designs of the power supply rails (V_{cc} and V_{dd}) and a few passive filtering components are omitted here (Figure S4). This power supply involves four direct current supply rails, where two of them are locally regulated. A pulse-width modulation (PWM) controller, TL494, was operated at 9 V (locally regulated from the V_{dd} rail). The output of the PWM controller was set to a 35% duty cycle. Ideally, the conduction angle should be minimal for a clean excitation of the L-C resonator in the driving transformer. We tuned the PWM controller to match the response time of the MOSFET gate driver, which was achieved by an NPN transistor in this case. The transformer was winded in-house, yielding a turn ratio of 1:20. The primary winding was specifically designed to match a 66 nF monolithic capacitor to achieve the L-C resonance at 40 kHz. No air gap was left in the transformer core.

The supply rail V_{cc} was set to 19 V through an SMPS (a common laptop power supply). The V_{cc} rail was then split into two: another adjustable SMPS for the V_{dd} rail, and into an inductor-capacitor series to the coupling transformer. Two local regulators were placed close to the PWM controller, and the Schmitt trigger IC (74HC14N), which regulated the V_{dd} down-to 9 V and 5 V, respectively. More detailed circuit design information is available upon request.

Practically, the transducers were driven through a common output. However, it requires all four transducers to match with each other. We purchased 200 transducers and experimentally selected four of them that exhibited highly similar impedance. Another solution is to design a driver that powers the four transducers through independent coupling transformers (similar to a phased array), which is beyond the scope of this work.

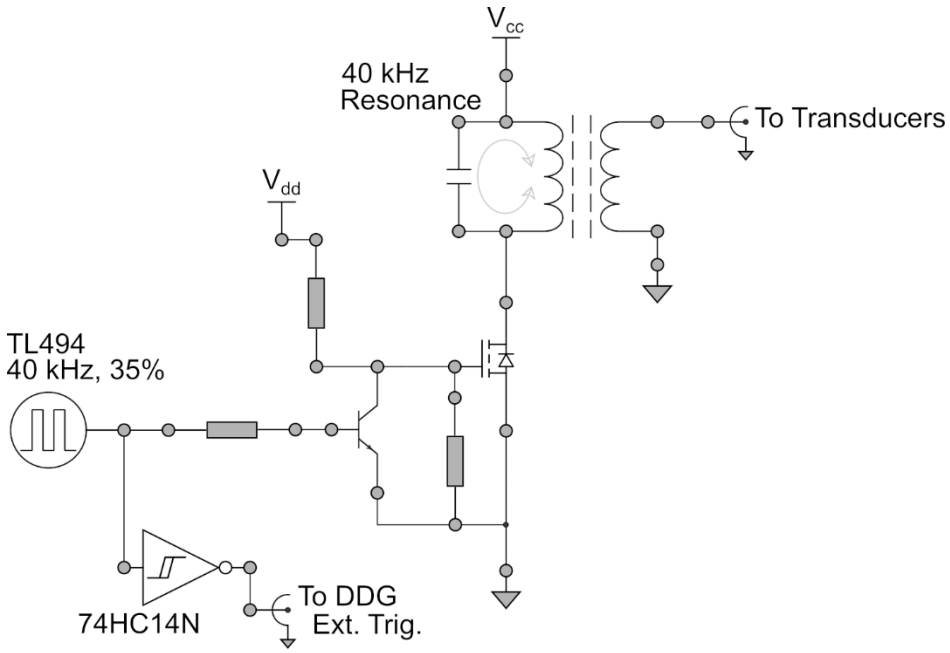

Figure S 4. Simplified schematic of the 2D acoustic resonator driver.

Home-made camera-lens assembly

The lens tube was designed in-house to be 100 mm in length, 30 mm inner diameter (to match with the outer diameter of the lens holder from Thorlabs), and 3 mm wall thickness, and was 3D-printed with polyethylene terephthalate glycol (PETG). The lens tube was printed to be oversized. Subsequent machining on a lathe with a specially made cutting bit ensured the smooth inner surface for lens travel. A metric scale with a resolution of 0.5 mm was attached to the lens-tube surface for rough estimations of the defocusing distance, $đ$,

Figure S 5. Lens tube and the camera.

2. Additional Data of Gas-Stream Visualization

For clarity, the raw images recorded with the knife-edge schlieren and defocusing-shadowgraphic imaging were given in Figure S6a and S6c, respectively. Note that the contrasts were adjusted to

enhance the flow features. In this extended section, we introduce another metric to compare the DF-shadowgraphy and knife-edge schlieren imaging, which uses the percentile change of the pixel intensity, expressed by:

$$V = \frac{\Delta I}{I} \times 100\% \qquad \text{Eq. S1}$$

where ΔI is the pixel-intensity difference with and without the gas stream; I is the pixel intensity without the gas stream. The percentage change serves as another metric in addition to the absolute intensity change (*i.e.* ΔI) given in the main text, specifically for the case when the outlet capillary was parallelly aligned with the knife-edge (Figure S6bd). For the example that the outlet capillary was perpendicularly aligned with the knife-edge (Figure S6ef), the absolute intensity change was used, same as the main text.

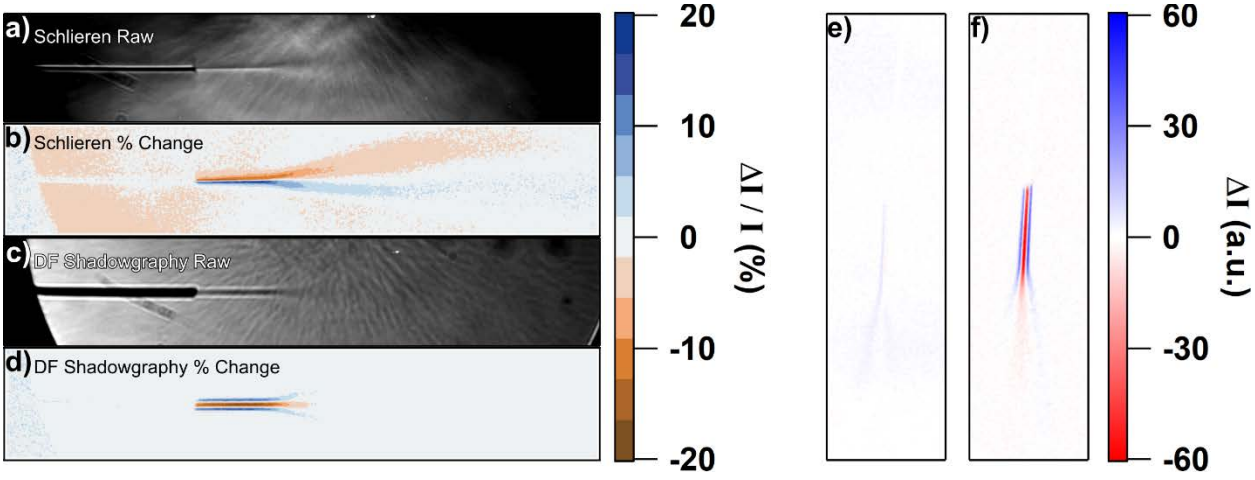

Figure S 6. Visualization of the isopropanol-containing gas stream with (a, b, e) knife-edge schlieren imaging and (b, d, f) defocusing (DF) shadowgraphy. The recorded images that were only contract-adjusted are given in (a) and (c). The percentage changes are given in (b) and (d) for schlieren and shadowgraphic imaging, respectively. The background-subtracted schlieren and shadowgraphic images of vertical gas stream are given in (e) and (f), respectively.

If the percentage change was used, the section views of the gas stream through DF-shadowgraphy and knife-edge schlieren imaging were comparable if the absolute maxima were used to assess the sensitivity (Figure S7). Importantly, the difference between the DF-shadowgraphy and the knife-edge schlieren imaging was not as pronounced as the absolute signal change, which is due to the cutoff of the knife-edge at the focal point. In our example, nearly half of the background light was blocked by the razor blade, which reduced the overall intensity of the schlieren image. However, we chose the absolute intensity change as the metric to assess and compare these two methods. One major reason is due to digitizing noise. For a digital detector, the signal variation corresponding to the sample change should cover a sufficient dynamic range to maximize the signal-to-noise ratio. Thus, even though the knife-edge schlieren and defocusing-shadowgraphic imaging showed similar sensitivity in terms of percentage intensity change, the usage of pixel

dynamic-range was drastically decreased due to overall light cutoff by the schlieren spatial filter; the dynamic-range reduction due to the spatial filter can be compensated by increasing the LED power or the gain/exposure of the camera. Moreover, the calculation of percentage intensity change involves a division operation with a background image. The use of absolute intensity change, where only subtraction is involved, can avoid the issue known as divide-by-zero. As such, the absolute signal change was used as the only metric throughout this work.

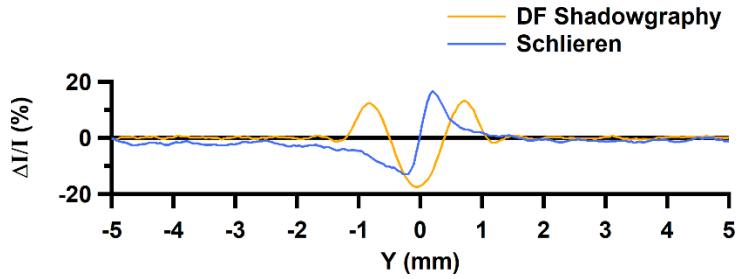

Figure S 7. Result section-views of DF-shadowgraphy and knife-edge schlieren imaging. The image size and aspect ratio are the same as that of Figure 1c for comparison.

3. Additional Data for Acoustic Resonators

Force analysis on a 1D acoustic resonator

From the later section of this work, it was found that the operations performed by the lens did not affect the spatial distribution if the IoR is primarily contributed by a single sinusoidal function (in space). However, it was also found that the intensity response to the IoR, or $\Delta I(n_s)$, is non-linear due to the convolution relation (Eq. 2). Thus, it would be difficult to determine the true value of acoustic force. Yet, a vector field can still be constructed to approximate the overall shape of the acoustic force field (Figure S8). Before a future work that focuses on the quantitative inversion of the IoR distribution in 3D space (here we only obtained the images as a 2D projection along the z-axis), the amplitude of the transient intensity change, $\Delta I(t)$ shown in Figure 2d, was used as-is to represent the pressure field. The vectors can then be calculated by:

$$\boldsymbol{f_{ac}} = \boldsymbol{\nabla} \mathrm{A}^2 \qquad \text{Eq. S2}$$

$$\Delta I(t) = \mathrm{A} \cdot \|\Delta I(t)\| \qquad \text{Eq. S3}$$

where $\boldsymbol{f_{ac}}$ is the acoustic force (vector) in the x-y plane; A is the normalization coefficient representing the amplitude of temporal pixel intensity, $\Delta I(t)$.

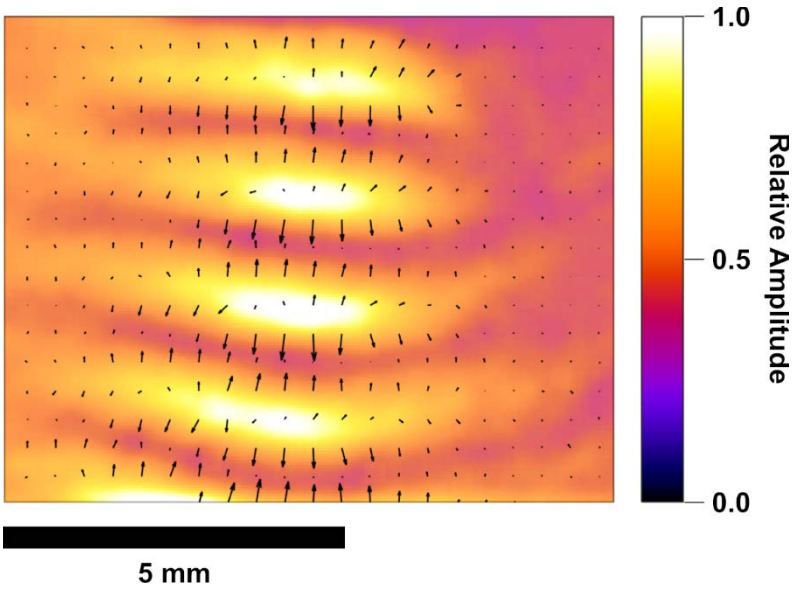

Figure S 8. 1D acoustic force field calculated by amplitude reconstructed image.

Image sequence of the 2D acoustic resonator in the reversed-phase mode

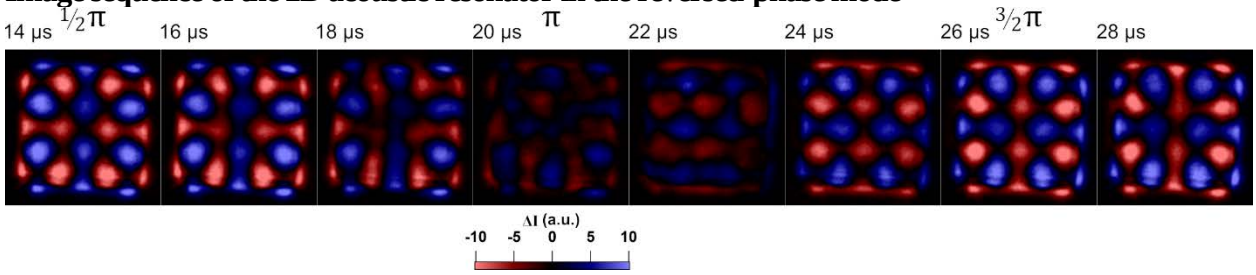

Figure S 9. Image sequence of the 2D acoustic resonator in reverse-phase mode with DF-shadowgraphy. The relative time marks and phase angles are labeled accordingly.

4. Extended Theoretical Approximation

Wavefront

A simplified expression of the wavefront, *U*, can be expressed by:

$$U(x,y) = Ae^{i\phi(x,y)} \qquad \text{Eq. S4}$$

where $U(x,y)$ is the 2D wavefront; A is the amplitude; and the monochrome form of $\phi(x,y)$can be found in the main text, Eq. 1. As a proof-of-concept study, the blue emission from the LED is treated as monochromatic light to avoid further complications. However, in terms of numerical computation, the non-monochrome wavefront can be written as a series:

$$U(x,y) = \sum_m \left\{ \|S(\lambda_m)\| \exp\left(i \int \frac{2\pi}{\lambda_m} (n_s(x,y) - n_{air}) dz \right) \right\} \qquad \text{Eq. S5}$$

where $S(\lambda_m)$ is the emission spectrum; the $\|S(\lambda_m)\|$ refers to as the normalized emission spectrum because the A-term in Eq. S4 is set to be 1; the term in the exponential function is the phase term as given in Eq. 1 in the main text. Note that this phase term is discrete for numerical computations as well. We left this phase term in an integral form to differentiate it from the wavelength series. Even though the light source was simplified to a monochrome one for simplicity, we do not deny that including the LED emission spectrum can improve the simulation accuracy.

To solve the numerical impulse response function, *h*, the wavefront was synthesized by two parts according to the gas-stream examples. The projection (or the shadow) of the capillary was assumed to only change the amplitude of the wavefront with no phase perturbation or $\phi(x, y) = 0$ (Figure S10a). A second segment that represents the gas stream contained only the phase perturbation without changing the amplitude, by assuming the zero-absorbance condition (Figure S10b). For gas-stream simulations (Figure 5 in the main text), these two segments were summed into the wavefront matrix. To derive the impulse response function, as stated in the main text, a slice on the capillary was used, where no phase perturbation existed in that region. Thus, the phase perturbation term was not involved. Moreover, the shadow of the capillary did not reach 0 counts on the detector. For improved simulation/optimization accuracy, the amplitude of the wavefront at the shadow of the capillary was set to be 0.2 instead of 0.

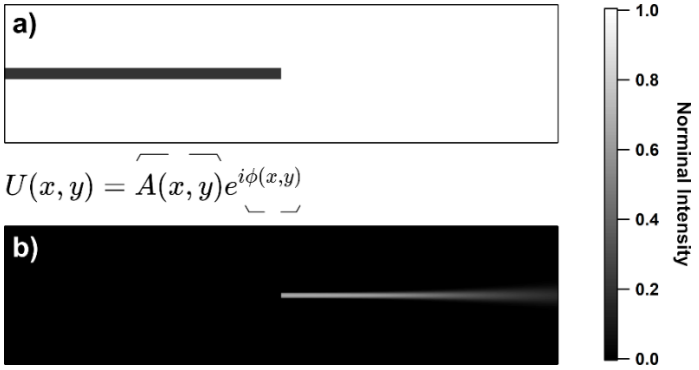

Figure S 10. Wavefront example for the numerical solution of the impulse response function and further simulations. The brackets shown in the symbolic wavefront equation indicate the amplitude component (a) and the phase perturbation (b). The color scale corresponds to the actual value in the matrix for (a) and (b).

Impulse response function

Subsequently, the wavefront is convoluted with the impulse response function to attain the detected intensity on the detector, $I(\tilde{x}, \tilde{y})$, Eq 2). The impulse response function, *h*, is a convolution of each optical component involved in the optical path: i) the sample that is placed between the mirror and the focal point; ii) the first spherical focusing lens at a certain distance to the focal point of the parabolic mirror; and iii) the second spherical focusing lens that is placed after the first lens and within its focal distance. Because the *h* is expressed numerically, the full symbolic expression is not given here. For simplicity, the short symbolic form of *h* is given in Eq. 2 in the main text, which is a convolution of a Gaussian term for image blurriness and a lens function that describes the lens geometry. The capillary as the target can be used to solve the impulse response function in 1D, which can be further expanded to 2D if center symmetry is assumed. The expanded expression of *h* in 1D that was used in this work can be given by:

$$h(x;đ) = e^{-\frac{(C_F\,(x-x_c))^2}{\sigma^2}} \otimes \frac{2\pi}{\lambda}(n_L - n_{air})L_c\{R - [R^2 - (C_F\,(x-x_c))^2]^{\frac{1}{2}} - \frac{1}{f_p}[(C_F\,(x-x_c))^2]\,\} \quad \text{Eq. S6}$$

where $h(x;đ)$ is the impulse response function at a defocusing distance $đ$; C_F is the conversion factor in the unit of px/mm; σ is the width of the Gaussian kernel; x_c is the x-offset to align the simulated and experimental slices; $n_L - n_{air}$ is the IoR difference between the BK-7 material and room air; L_c is the lens correction factor, which is designed to compensate the error in the estimated Δn; R is the equivalent radius of the combined focusing lens, which consists of two spherical lenses; f_p is the focal length of the parabolic mirror. Note that the convolution symbol was left as-is instead of being written into a form of Fourier transform for simplicity. The parameters that are to be optimized are marked with color codes: black indicates preassigned values that are not optimized; the blue ones are scaling/conversions factors in the length dimension; the red ones are system parameters that are to be optimized. The equivalent radius, R, of the focusing lens was estimated based on the equation:

$$\frac{1}{f} = (n_L - n_{air})\frac{1}{R} \quad \text{Eq. S7}$$

where f is the focal length.

Because the Nelder-Mead simplex method exhibits problems with local minima, the parameters marked in red were selected close to the real dimension, whereas the blue terms were arbitrarily chosen. We chose the Nelder-Mead simplex method (or fminsearch in Matlab) is because of the non-derivative nature of this approach. Meanwhile, the Nelder-Mead method does not require optimization bounds, which is quite convenient in our case because both the conversion factor and the lens correction factor were difficult to determine experimentally.

Importantly, the intensity correction factor, κ (Eq. 2), was not included in the optimization process. The impulse response function, h, and the given wavefront, U, are normalized quantities. Thus, the optimization and determination of the numerical impulse response function were based on the normalized pixel intensities, or $\|I(\tilde{x},\tilde{y})\|$. Thus, the nature of the intensity correction factor, κ, is merely the normalization constant for the pixel intensities of an experimental image. Additionally, a magnification factor, M, was introduced for the final scaling of the simulated image and the experimental one:

$$\tilde{x} = \frac{x}{M}; \tilde{y} = \frac{y}{M} \quad \text{Eq. S8}$$

List of optimization parameters

In Table S1, all parameters that were optimized for solving the numerical expression of h were given. Importantly, many correction/conversion factors were included in the optimization process. For instance, the experimental dimension relationship between the experimental geometry and pixel sizes in an image can be reflected by the product of conversion factor and magnification factor, yielding a 0.412 mm/px projection ratio. Similarly, the parabolic focal length, f, and the

equivalent lens radius, R, can be reflected by their products with the lens correction factor, L_c. Namely, many of the unitless parameters were redundant. However, involving these conversion factors improved the overall optimization accuracy.

As stated in the main text, the impulse response function needs to be calculated only once for a specific setup, which means that the parameters that describe the camera position, defocusing distance, and the light source condition should be maintained. Any change in these parameters requires recalculating the numerical impulse response function, even though the computation is not at all time-consuming. The fitness function, which describes the difference between an experimental image and a simulated one, involves convolution. In this work, the convolution was computed through fast Fourier transform. An image is zero-filled to the minimal radix-2 matrix that is larger than the image itself. For instance, the raw image (2560 px × 1920 px) was zero-filled to 4096 px × 4096 px. This zero-filling step can be obviated if Matlab or similar software is used.

Table S 1. Parameters and constants to numerically solve for the impulse response function. All numbers are given in text format of "general 4 digits" or "G4".

Name/Type	Symbol	Unit	Initial Guess	Optimized Result
Gaussian Width Variable	σ	px	10.00	10.35
Conversion factor Variable	C_F	mm/px	0.1000	0.2022
Equivalent Lens Radius Variable	R	mm	87.50	78.72
Parabolic Focal Length Variable	f_p	mm	1200	1178
Lens Correction Factor Variable	L_c	1	1	1.076
Magnification Factor Variable	M	1	2	2.038
Center Offset Variable	x_c	px	900	954.9
Wavelength Constant	λ	nm	470	N/A
IoR of Air Constant	n_{air}	1	$1+2.930\times10^{-4}$	N/A
IoR of BK-7 Constant	n_L	1	1.517	N/A
IoR of Sample *Constant	n_s	1	Vary	N/A
Capillary O.D. Measured Constant	N/A	in.	1/16	N/A
Capillary O.D. In Simulation Constant	N/A	px	21	N/A
Defocusing Distance Constant (unused)	đ	mm	2	N/A

Pupil function

In the main text, the numerical solution (in the form of complex matrix) of the impulse response function is given (Figure 4). Both the vertical slice (Figure 4b) and 2D representations (Figure 4cd) were truncated to show the key features near the reference target, *i.e.* the outlet capillary. The term, pupil function, is also omitted in the main text for simplicity. However, the pupil function that cut off the edge of the numerical impulse response function was involved during the computation. In this study, the pupil function was used to truncate the impulse response function to remove the artifact near the edges (Figure S11). The pupil function used in this study merely truncated the edges of the numerical impulse response function without any physical representations of any dimensions.

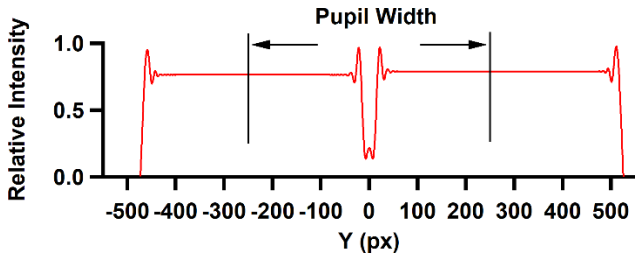

Figure S 11. Full vertical slice of an impulse response function corresponding to the dataset shown in Figure 4. The pupil function is noted graphically as the pupil width, marked by solid-black traces.

5. Gas-Stream Simulation

As indicated by the main text and the SI, section 4, the phase perturbation was constructed based on a base term, which is a 2D projection of a cylinder with a diameter corresponding to the inner diameter of the outlet capillary (Figure S12a). A subsequent spreading term was later composed with the cylindrical projection (Figure S12b). Empirically, a third-order polynomial was used to describe the gas spreading as a function of the travel distance from the outlet capillary. The origin is defined at the exact location at which the capillary ends. That is, the gas profile was set to zero for all $X < 0$, whereas for $X \geq 0$, the base of the gas stream was set to the same for all X as shown in Figure S12a.

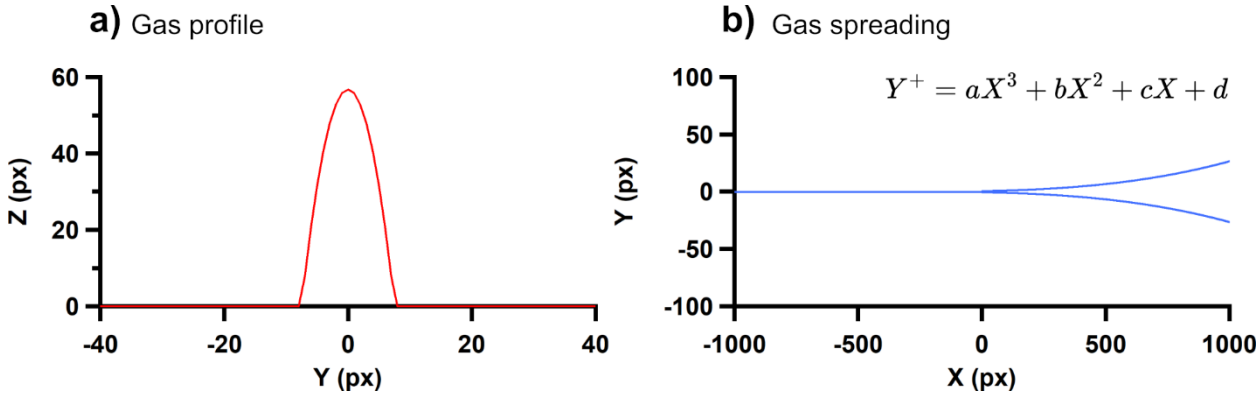

Figure S 12. Simulation of the gas stream and its spreading on the travel. A vertical slice is given in (a). The gas spread function is given graphically in (b).

To obtain a flow pattern shown in Figure S10b, each vertical slice of the base was convoluted with a Gaussian kernel. If the positive branch of the gas-spreading function is defined as Y^+, the negative branch can be expressed by Y^- (Figure S12b). Then, the σ of the Gaussian kernel for each pixilated X can be expressed by $Y^+ - Y^-$. The synthetic image is then the map of optical depth, or the z term in Eq. 1 and Eq. S5; this means we assumed that the IoR of a sample, n_s, is not a function of z.

The empirical formula of the gas-spreading function was determined by fitting the edge of the flow pattern shown in Figure S6 based on isopropanol/air and acetone/air mixtures. The flow pattern can vary depending on the type of gas and the exact flow rate. Based on the comparisons between

the simulated and experimental slices of various gases (Figure 5), the accuracy of the gas-spreading model appeared to be sufficient when the slicing coordinate is close to the gas outlet.

In addition to the flow images shown in Figure S6c for isopropanol/air mixture, and Figure 5a for acetone/air mixture, the raw images in accordance with Figure 5 are given in Figure S13.

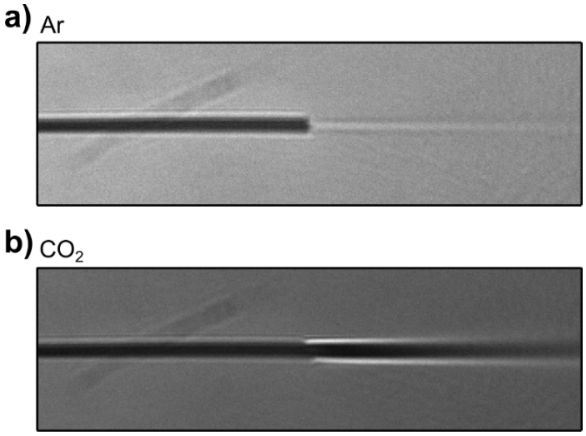

Figure S 13. Additional experimental images of argon (a) and CO_2 (b).

6. Justification for Acoustic-Field Mapping

The results from the gas stream study implied the fundamental principle of imaging the phase perturbation is strongly related to the wavelet transform. The wavelet transform itself is quite commonly used in peak detection algorithms because of its capability of enhancing localized features. However, the advantage of wavelet transforms inherently suggested that spatial features that span over a large area will be inhibited to or close to zero, such as the gas-stream features at further distances to the outlet capillary. In contrast, for fine features that are significantly narrower than the span of the wavelet kernel, the wavelet transform behaves closer to smoothing. As such, the applicable range for acoustic-field mapping should exhibit two boundaries: the acoustic wavelength should not be too long to be inhibited, nor to be too short that the impulse response function overly smooths the localized features.

Given the experimental conditions in this study, where the acoustic wavelength is either 4.25×2 mm (40 kHz) or 3.04×2 mm (56 kHz), the simulated results indicated that the observed image should resemble the features of the phase perturbation induced by sounds (Figure S14). Here, a frame (synchronous mode) of the acoustic field at 40 kHz was calculated, where the corresponding phase perturbation can be obtained (Figure S14a). Because the transient acoustic field was simulated in this example, the amplitudes contained both positive and negative parts. Taking the phase term into Eq. 1 or Eq. S5 at 470 nm yielded the wavefront. Note that the exact numbers used here merely demonstrate the preservation of spatial features instead of inverting the absolute pressure distribution of the acoustic field, even though the pressure distribution can be calculated. To obtain the expected image on the detector, the intensity matrix or $I(\tilde{x}, \tilde{y})$, was calculated with Eq. 2, where the impulse response function of at $\tilde{d} = 2$ mm derived from the gas-stream example was used (Figure S14b). Note that the intensity correction factor was omitted here by setting κ to 1. Aside from the apparent similarity between the phase-perturbation map (Figure S14a) and the

expected intensity distribution (Figure S14b), vertical slices of both images at X = 0 mm were plotted together (Figure S14c) for a more direct comparison. Despite the inaccuracies at the edges (mainly due to the discrete Fourier transform), the expected image indicated that the optical operation of DF-shadowgraphy preserved the phase-perturbation distribution. As such, we claim that the DF-shadowgraphy can be used as-is if an acoustic field is to be mapped.

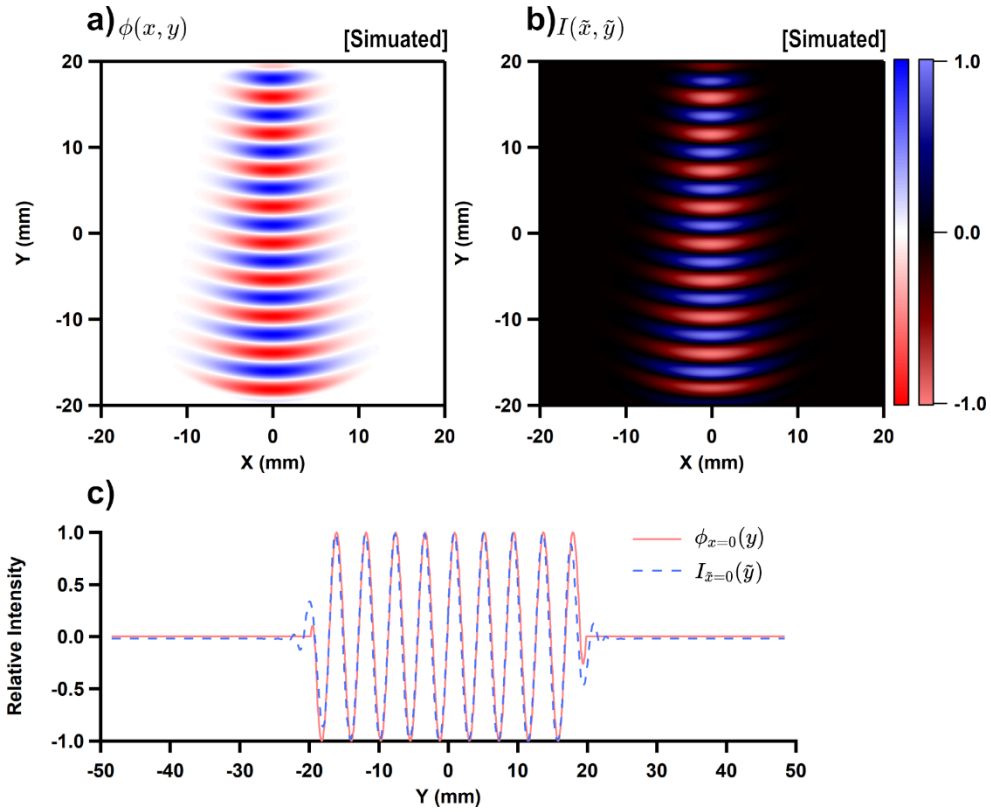

Figure S 14. The transient phase perturbation induced by the 40-kHz ultrasound (a) and the expected image at the detector (b) are given with color codes. To differentiate these images, two color-codes are used as given in the color bar. The vertical slices of the images at X = 0 mm were plotted together for comparisons (c).

The acoustic frequencies used in this study resulted in images that can directly reflect the acoustically induced phase perturbations. However, as stated previously, the wavelet nature of the impulse response function may clutter the resulting image if the spatial features are too widely spanned or too fine. Following the same routine of computing the expected image from a synthetic phase-perturbation distribution (*i.e.* changing the acoustic frequency for Figure S14a), we report that the expected images show the same degree of agreement to the phase-perturbation distribution as given in Figure S14c between the range of 23 kHz to 75 kHz (data not shown). The system parameters (*e.g.*, λ and $đ$) must be tuned to interpret phase perturbations at acoustic frequencies beyond this range. Alternatively, inversions must be performed. Namely, beyond the acoustic frequency range of 23-75 kHz, the images from the DF-shadowgraphy can no longer be used as-is.

7. Impulse Response as a Function of Defocusing Distance, đ

The optical geometry allows only one tunable parameter, which is the defocusing distance, *đ*. At *đ* = 0 mm, a sharp image is expected as for the conventional shadowgraphy. At *đ* > 0 mm, the phase perturbation starts to appear. Experimentally, the isopropanol/air mixture images were recorded at different *đ* (Figure S15). Due to the manual focusing, we were unable to achieve a true *đ* = 0 mm condition. Consequently, a weak flow pattern was still observed even at *đ* = 0 mm (Figure S15). Further moving the lens towards the camera, or increasing the *đ*, yields blurry and magnified images (Figure S15). Upon careful inspection, the sensitivity as a function of *đ* appeared to increase from *đ* = 0 mm, reached a maximum, and decrease as *đ* further increased.

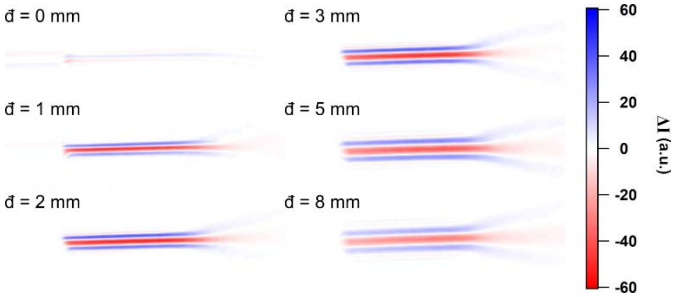

Figure S 15. Background-subtracted images of isopropanol/air gas stream at different defocusing distances, đ.

Instead of absolute intensity, *I*, the relative change, *ΔI/I* (Eq. S1) was used as a metric to describe the sensitivity of the setup as a function of defocusing distance *đ* (Figure S16, red-solid trace and circle markers). As the *đ* increased, the recorded image magnified, which means less light reached the same detector area. As such, the relative intensity change is a better metric than the absolute one. Additionally, the image blurriness was described by the Gaussian term within the impulse response function, where the σ was used as a metric (Figure S16, blue-solid trace and square markers). More specifically, the sensitivity term was determined by the center point of the gas stream in different images 2.5 mm away from the outlet capillary. The pixel position is not given here due to the change of magnification factor. Meanwhile, the σ term was determined while deriving the *h*-matrix, as the *σ* is one of the optimization parameters. To generalize the trend of the sensitivity and the image blurriness as functions of đ, the experimentally determined points (noted by markers in Figure S16) were connected by polynomials. Up until this point of the work, no model is built to mathematically describe the relationship between the sensitivity and image blurriness as functions to *đ*. Nonetheless, the practically determine *đ* = 2 mm condition appeared to be close to the maximum sensitivity, at the cost of σ at ~14 px.

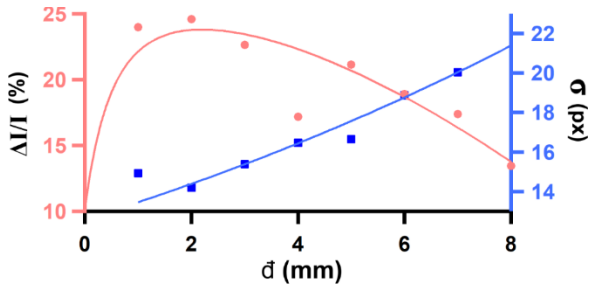

Figure S 16. The sensitivity and image blurriness as a function of defocusing distance, đ. The red and blue markers are the experimentally derived values. The circles and squares represent the sensitivity given by the relative intensity change and the σ term of the Gaussian component in the impulse response function, respectively.

Importantly, if the *h* is considered a complex kernel for a wavelet transform, a greater *đ* means that the impulse response of the system is less sensitive to the localized spatial features, but quite sensitive to those that span over a greater area. If the images at *đ* = 1 mm and *đ* = 8 mm are compared (Figure S16), the latter showed clearer features after the laminar region of the gas stream. In general, the *đ*, as the only tunable parameter in the optical system, can be based as a modulator to map a phase-perturbation distribution at different conditions. In addition to the wavelength of the light source, a second dimension, *i.e.* đ, can also be adjusted and used as a mean for absolute measurement of the phase perturbations.